Superhydrophobicity enhancement through substrate flexibility

Thomas Vasileiou[a], Julia Gerber[a], Jana Prautzsch[a], Thomas M. Schutzius[a,1], and Dimos Poulikakos[a,1]

[a]Laboratory of Thermodynamics in Emerging Technologies, Department of Mechanical and Process Engineering, Eidgenössische Technische Hochschule Zürich (ETH Zürich), CH-8092 Zurich, Switzerland

Edited by David A. Weitz, Harvard University, Cambridge, MA, and approved October 11, 2016 (received for review July 18, 2016)

Inspired by manifestations in nature, microengineering and nanoengineering of synthetic materials to achieve superhydrophobicity has been the focus of much work. Generally, hydrophobicity is enhanced through the combined effects of surface texturing and chemistry; being durable, rigid materials are the norm. However, many natural and technical surfaces are flexible, and the resulting effect on hydrophobicity has been largely ignored. Here, we show that the rational tuning of flexibility can work synergistically with the surface microtexture or nanotexture to enhance liquid repellency performance, characterized by impalement and breakup resistance, contact time reduction, and restitution coefficient increase. Reduction in substrate areal density and stiffness imparts immediate acceleration and intrinsic responsiveness to impacting droplets (~350 × *g*), mitigating the collision and lowering the impalement probability by ~60% without the need for active actuation. Furthermore, we exemplify the above discoveries with materials ranging from man-made (thin steel or polymer sheets) to nature-made (butterfly wings).

droplet impact | superhydrophobicity | flexible | wetting transition | biomimicry

Hydrophobic surfaces have gained much attention in recent years (1) for their unique attributes, such as self-cleaning behavior (2), extreme repellency to liquids (3, 4), and resistance to surface icing (5). For practical applications, repellency to impacting liquid droplets is of great importance, and numerous studies have investigated the physics of droplet impact on rigid surfaces and the diverse outcome of such events for a broad range of liquid properties and impact conditions [liquid viscosity (6, 7), surface tension (3), environmental pressure (8, 9), etc.]. Additionally, extensive work has been done on the role surface morphology plays in determining the outcome of such events—with the goal being full rebound of an impacting droplet from the surface (10–17). In these studies, the emphasis was on texturing rigid materials to impart enhanced properties. On the other hand, there is a broad palette of surfaces in nature and technology that is characterized by some degree of flexibility [leaves (18), construction materials, textiles (19), etc.]. Studies have been reported with respect to dynamic wetting on hydrophilic, flexible materials (20–23); however, little work has addressed the interweaving effects of wetting behavior and material flexibility. In addition, the work that has been reported (24) did not focus on the role of surface compliance or flexibility in influencing the physics of the droplet collision process.

Here, we investigate the effect of substrate flexibility on superhydrophobicity through the outcome of droplet impact events with respect to impalement resistance, droplet–substrate contact time, maximum droplet deformation, and restitution coefficient. We demonstrate, through appropriate modeling and experiments, that, by rational tuning of the substrate stiffness and areal density, flexibility can actually work collaboratively with superhydrophobicity to significantly extend the range of performance in terms of droplet impalement resistance, breakup inhibition, contact time reduction, and restitution coefficient enhancement. Moreover, we show the manifestation of extended water repellency due to substrate flexibility in natural surfaces, specifically on butterfly wings. In general, this work shows and explains the important role that the (routinely) overlooked effect of substrate flexibility can play in setting the dynamic wetting behavior of superhydrophobic surfaces with practical consequences for diverse applications.

Results

Impalement Resistance. As a flexible hydrophobic substrate, we used a low-density polyethylene (LDPE) film treated with a hydrophobic nanocomposite (nC1) coating. The selected coating exhibits low-impalement resistance, facilitating a clear comparison between the rigid and the flexible cases without introducing complications arising from high droplet impact velocities (e.g., splash). [For complete information regarding the coatings (nC1 and nC2), see *Wettability Characterization*, Fig. S1, Table S1, and *Coating Preparation*.] To assess the role of substrate compliance ($1/k$) on the dynamic wetting behavior of the surfaces, we sectioned films into 30 mm × 10 mm pieces, clamped them at both ends along their long side without introducing any pretension, and impacted water droplets of diameter $D_0 = 2.35$ mm on them. The droplet impact velocity (U_0; direction normal to the surface) and Weber number, $We = \rho U_0^2 D_0/\sigma$, were kept constant during the experiments ($We = 50$), where ρ is the density and σ is the surface tension of the liquid droplet.

For a better comparison between the rigid and flexible substrates, we used a paired experimental design; the same surfaces and impact locations were used for both cases. To attain substrate rigidity we used a glass backing under the sample. Image sequences of a droplet impacting on an LDPE film for both the flexible (suspended) and rigid (backed) cases are shown in Fig. 1*A* (see also Movie S1), as a function of the inertial capillary time, $\tau = \pi/4\sqrt{\rho D_0^3/\sigma}$; τ is the

Significance

Flexible materials are ubiquitous in everyday life and technology; however, their effect on wetting dynamics is not well understood. We explore the related physics and whether substrate flexibility can be made to work synergistically with surface microtexturing and nanotexturing to enhance superhydrophobicity. Remarkably, we show that, depending on substrate areal density, stiffness, and damping, a tunable collaborative effect of elasticity and superhydrophobicity can be realized. We identify the mechanism responsible for this enhancement with a simple collision model, and we propose design criteria for promoting this behavior. We exemplify the above discoveries, with materials ranging from man-made (thin steel or polymer sheets) to nature-made (butterfly wings).

Author contributions: T.M.S. and D.P. designed research; T.V., J.G., and J.P. performed research; T.V. and J.G. analyzed data; and T.V., J.G., T.M.S., and D.P. wrote the paper.

The authors declare no conflict of interest.

This article is a PNAS Direct Submission.

[1]To whom correspondence may be addressed. Email: dpoulikakos@ethz.ch or thomschu@ethz.ch.

This article contains supporting information online at www.pnas.org/lookup/suppl/doi:10.1073/pnas.1611631113/-/DCSupplemental.

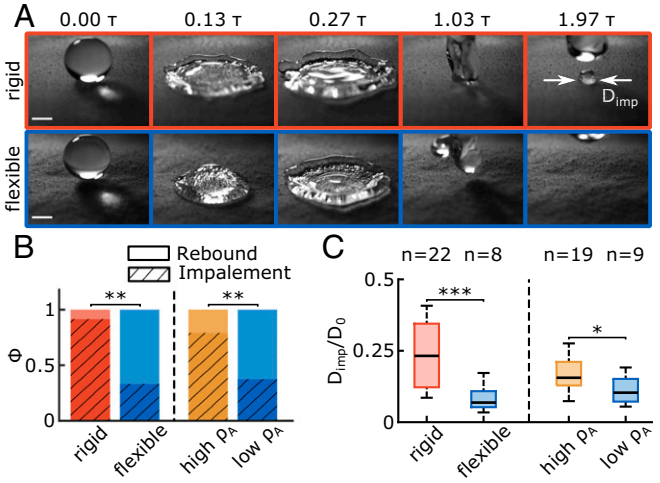

Fig. 1. Comparison of impalement resistance between rigid and flexible/high areal density substrates. (*A*) Image sequence showing a droplet ($D_0 =$ 2.35 mm, $We =$ 50) impacting on rigid (*Upper*) and flexible (*Lower*) superhydrophobic surfaces (nC1 coating). (Scale bar, 1 mm.) (*B*) Probability of impalement (Φ, hatched) and full rebound ($1 - \Phi$, filled) for droplet impacts on the rigid and flexible substrates (left, $D_0 =$ 2.35 mm, $We =$ 50, $n =$ 24) and flexible substrates with low and high areal density (right, $D_0 =$ 2.35 mm, $We =$ 69, $n =$ 24). (*C*) Relative diameter of impalement zone (D_{imp}/D_0) in the case where impalement did occur during the droplet impact event. Data correspond to the impalement events depicted on *B*. Box spans from the first to third quartile with Tukey style whiskers, and bold lines indicate population medians. Sample size (n) is indicated above each box. Significant differences are indicated by asterisks (*$P < 0.05$; **$P < 0.01$; ***$P < 0.001$).

natural oscillation period of a vibrating droplet (25). For the flexible substrate, when the droplet rebounds, no impalement into the texture is detected, whereas, in the rigid case, partial rebound left a pinned droplet on the surface. This signifies the displacement of the air layer out of the surface asperities by the penetrating liquid meniscus, the so-called Cassie–Baxter to Wenzel wetting transition (16), resulting in loss of droplet mobility. Two quantities were measured from the videos and are shown on the left side of Fig. 1 *B* and *C*, respectively: the presence of remaining liquid adhering to the surface (probability of observing the Cassie–Baxter to Wenzel wetting transition, Φ; see *Impalement Probability Measurement*) and the impalement parameter, D_{imp}/D_0, where D_{imp} is the impaled droplet–substrate diameter. To elucidate the postimpalement dynamics, Fig. 1*C* reports D_{imp}/D_0 only for cases where impalement did occur ($D_{imp}/D_0 > 0$). Overall, for the flexible substrate, compared with the rigid case, a 58% reduction in Φ is estimated, and, when droplet impalement does occur, D_{imp}/D_0 is significantly reduced. Both these results support a marked effect of substrate flexibility on enhancing impalement resistance.

Although flexibility has a positive effect on superhydrophobicity, we hypothesized that the substrate mass per unit area (areal density, ρ_A) should also play a critical role in the process. We repeated the above experiments with high and low ρ_A, flexible substrates keeping all other parameters constant (e.g., $D_0 =$ 2.35 mm, $We =$ 69). For the low-ρ_A case, we used the same coated LDPE film as before; to increase ρ_A for such a surface, *ceteris paribus*, we simply placed a liquid droplet—~10 times larger mass than the impacting droplet—on the uncoated, wetting backside of the LDPE film. Both Φ and D_{imp} are plotted on the right side of Fig. 1 *B* and *C*. Similarly, we observed a decrease in both Φ (~40% reduction) and D_{imp}/D_0 (~34% reduction) for the low-ρ_A substrates in comparison with the high-ρ_A ones. The behavior of the latter tends toward that of the rigid superhydrophobic surface.

We conjecture that the mechanism behind the improved water repellency in the high $1/k$ and low ρ_A case is related to the relative movement between the surface and the droplet in the early stages of impact that are critical to the impalement process (14). This effect can be quantified by measuring the substrate velocity, U_s. We impacted droplets with $D_0 =$ 2.35 mm and $We =$ 50, and we measured U_s using a laser vibrometer. Moreover, we recorded video sequences in sync with U_s acquisition. Adding a droplet to the backside of the film would hinder the vibrometer reading; therefore, we used a steel substrate of thickness $h_b =$ 10 μm. We formed a beam with width $W_b =$ 8 mm and length $L_b =$ 62.5 mm, and we treated it with the same hydrophobic coating (nC1). We fixed it on one end and simply supported it at a distance of $L_s =$ 30 mm (Fig. S2*B*). During our experiments, for droplet impact events on the metal beam, we found $\Phi \approx 1$; for the LDPE film, $\Phi \approx 0.33$, which matches the result reported earlier (Fig. 1*B*).

Fig. 2*A* shows a plot of the normalized substrate velocity U_s/U_0 vs. time, t, where $t =$ 0 signifies the moment of droplet–substrate contact (see also Movie S2). For the LDPE film, U_s is always higher than the steel beam at this initial impact stage. The time needed for the LDPE film to go from 10% to 90% of its plateau value is approximately one-third of the one for the steel beam. The LDPE film accelerates faster and reaches $U_s/U_0 \approx$ 0.12 just before impact, reducing the apparent impact velocity. Specifically, we detected motion of the substrates even before contact with the droplet, likely due to the compression of the air layer above the surface. Such compressed air layers have been demonstrated for droplet impact on rigid surfaces (26, 27). Therefore, we assume that, just before contact, action–reaction

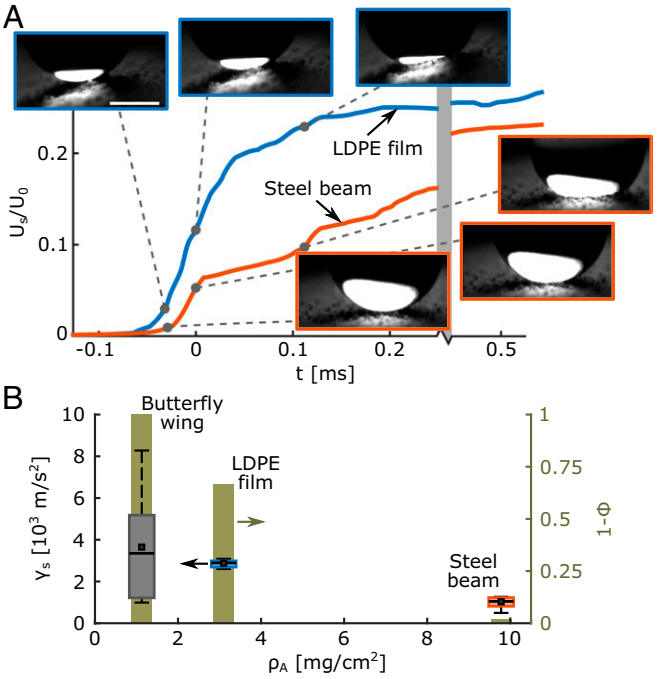

Fig. 2. Substrate velocity and acceleration during impact. (*A*) Normalized substrate velocity profile (U_s/U_0) versus time as recorded by the laser vibrometer at the early stages of the impact event ($D_0 =$ 2.35 mm, $We =$ 50) for the LDPE film (blue) and steel beam (red). Time zero is set to the instance of contact. Both surfaces are treated with coating nC1. (*Insets*) Snapshots for three time instances, just before contact, at $t =$ 0, and at $t =$ 112 μs. (Scale bar, 1 mm.) (*B*) Mean substrate acceleration (γ_s, box plot corresponding to the left axis) just before the moment of impact and probability of total rebound ($1 - \Phi$, bar plot corresponding to right axis) versus substrate areal density (ρ_A), for the same impact conditions as in *A*. Box spans from the first to third quartile with Tukey style whiskers, bold lines indicate population medians, and square markers denote the population means. Sample size (n) is 5 repetitions per substrate for estimating γ_s and 24 repetitions per substrate for estimating $1 - \Phi$.

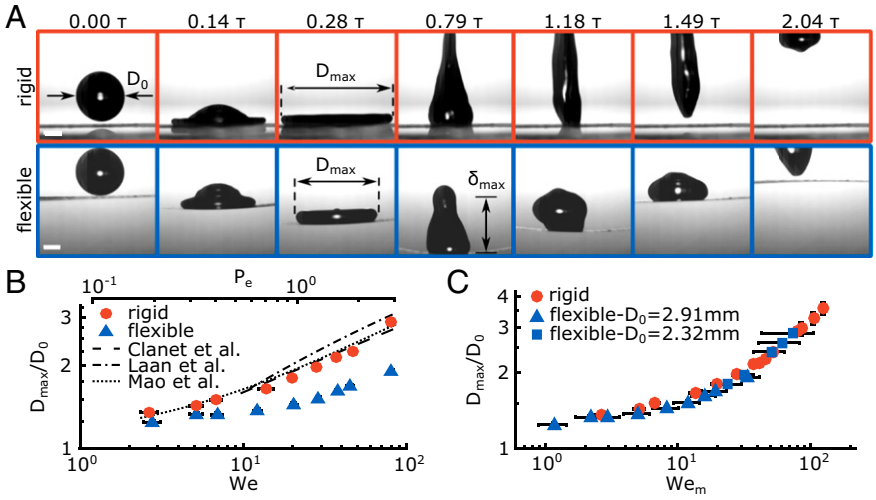

Fig. 3. Droplet spreading on flexible substrates. (*A*) Image sequences of droplet ($D_0 = 2.91$ mm) impacting on flexible and rigid hydrophobic substrates (steel beam treated with nC2). The maximum spreading diameter is indicated on the images as D_{max}. (Scale bar, 1 mm.) (*B*) Spreading parameter (D_{max}/D_0) for different values of *We*. Lines indicate the predicted values for D_{max}/D_0 using three theoretical models for their validity range: Clanet et al. (6) (dashed line), Laan et al. (28) (dash-dotted line), and Mao et al. (40) (dotted line). P_e of the impacts is indicated by the second horizontal axis. (*C*) D_{max}/D_0 plotted vs. We_m for the rigid (circle) and flexible cases for two droplet sizes (triangle, $D_0 = 2.91$ mm; square, $D_0 = 2.32$ mm). Sample size (*n*) for *B* and *C* is five repetitions per point. Error bars represent ±99% confidence interval of the mean. Nonvisible error bars are smaller than the marker size.

forces, which are mediated by the intervening air layer, are exerted between the substrate and the droplet. From this, ρ_A should be inversely proportional to the substrate downward acceleration (γ_s) and therefore proportional to Φ.

We estimated the mean γ_s just before contact for three substrates with varying ρ_A. This was achieved by using different materials, namely, butterfly wings (~1 mg·cm^{-2}), LDPE (~3 mg·cm^{-2}), and stainless steel (~10 mg·cm^{-2}). The results are shown in Fig. 2*B* alongside with the probability of rebound, $1-\Phi$; we used $1-\Phi$ instead of Φ to facilitate inspection. Indeed, we discovered that $\gamma_s \propto 1/\rho_A$ and $\gamma_s \propto 1-\Phi$; the surface with the smallest ρ_A demonstrated $1-\Phi = 1$, whereas the highest value of ρ_A led to $1-\Phi \approx 0$. To further elucidate the mechanism responsible for accelerating the substrate, we estimated the pressure exerted on the substrate at $t = 0$ as $p_a = \rho_A \gamma_s$. We scaled p_a with the Laplace pressure of the droplet, $p_\sigma = 4\,\sigma/D_0$, and it yielded a range of values of p_a/p_σ from 0.33 to 0.79 with increasing ρ_A from left to right. We see that the overpressure in the intervening air layer is of the same scale as p_σ. In this region, one would expect minimal deformation of the droplet-free surface and efficient energy conversion from droplet kinetic energy to substrate kinetic and strain energy. Physically, this makes sense due to the low areal density ($\rho_A << \rho D_0$) and low stiffness (k) of the substrate compared with the droplet (e.g., droplet with $D_0 \approx 2.5$ mm impacting on an LDPE film). Regarding k, for a given applied force, comparable substrate and droplet deformation is expected when $k \approx \sigma$. The estimated values for the steel beam and LDPE film were found to be ~0.5 N·m^{-1} and ~0.042 N·m^{-1}, respectively (see *LDPE Film Modeling*, *Beam Modeling*, and Fig. S3), supporting that $k \approx \sigma$ for improved impalement resistance. Finally, to achieve a high value of γ_s, one should also consider the damping ratio of the substrate, $\zeta = \pi f_s\, c/k$, with the goal being to minimize it, where f_s is the natural frequency of oscillation of the substrate and c is the damping coefficient. It has been shown that the main contribution to c comes from air (24), indicating that the effects associated with the substrate are at a minimal state. Stated succinctly, to maximize $1-\Phi$, one should maximize γ_s, which can be achieved by satisfying the following conditions: $\rho_A << \rho D_0$, $k \approx \sigma$, and $\zeta \approx 0$.

Spreading Parameter. We quantified the effect of k on the droplet spreading parameter, defined as the ratio of the maximum and initial droplet diameters (D_{max}/D_0), using a steel beam treated with the hydrophobic coating nC2. The coating nC2 exhibits high impalement resistance, allowing one to study the effect of substrate flexibility on droplet impact dynamics (e.g., spreading parameter) for a wide-range of *We*. The dimensions of the beam were $h_b = 10$ μm, $W_b = 8$ mm, $L_b = 62.5$ mm, and $L_s = 30$ mm. We characterized the beam using its natural frequency of oscillation, f_b, the flexural rigidity, k_b, and its effective mass, $m_b = k_b/(2\pi f_b)^2$ (see *Beam Modeling*). This configuration resulted in a beam with $f_b = 36$ Hz and $m_b = 9.5$ mg. We impacted droplets with a fixed diameter ($D_0 = 2.91$ mm). To vary *We*, we changed the release height of the droplet. Fig. 3*A* shows an image sequence of impacts onto a rigid and flexible substrate; substantial reduction in D_{max}/D_0 was observed for the latter case (see also Movie S3). Although D_{max} was achieved in both cases at the same time instance after droplet–substrate contact, the downward movement of the flexible substrate decreases the relative impact velocity—reducing the crashing force—resulting in a smaller D_{max}/D_0. Fig. 3*B* presents a plot of D_{max}/D_0 versus *We*. For the rigid case, our results are in good agreement with three theoretical models for their validity range (see *Model for Maximum Spreading*). In Fig. 3*B*, we show the impact number (28) $P_e = We\, Re^{-0.4}$ in a second axis, where $Re = \rho D_0 U_0/\mu$ is the Reynolds number and μ is the dynamic viscosity of the fluid. Note that, for a given D_0, the relation between *We* and $P_e = We^{0.8}\mu^{0.4}/(\sigma\rho D_0)^{0.2}$ is one to one (surjective).

For the flexible case, the reduction in D_{max}/D_0 is evident for the whole range of *We*, and it resembles a shift toward the right (higher *We*). We postulate that the droplet perceives the downward movement of the flexible substrate as a reduction in the apparent *We*. This reduction in *We* can be quantified by calculating the mean acceleration experienced by the droplet during spreading, γ_d, as has been demonstrated previously by Clanet et al. (6) for a rigid surface. Following the same analysis, we calculated γ_d experienced by the droplet in the reference frame moving with the surface. For $f_b < 1/\tau$, the substrate velocity just after impact, U_{s0}, scales as the one for a perfectly inelastic collision (23, 24), $U_{s0} \approx U_0 m_d/(m_b + m_d)$, where m_d is the mass of the droplet. The droplet experiences a deceleration from $U_0 - U_{s0}$ to 0; when D_{max}/D_0 is achieved, the droplet is immobile with respect to the substrate. The spreading takes place in the crashing time, which is of the order of D_0/U_0 (6), independent of the presence of compliance or not, resulting in $\gamma_d \approx U_0^2/D_0[1 - m_d/(m_d + m_b)]$. For the spreading dynamics, the droplet impact can be described by a modified *We* number, defined as

$$We_m = We\left(1 - \frac{m_d}{m_d + m_b}\right). \quad [1]$$

We see from Eq. **1** that, for substrates with $m_b >> m_d$, the difference between *We* and We_m diminishes, and it is eliminated in

the rigid case. By using We_m to plot D_{max}/D_0, all data collapse onto a single curve as shown in Fig. 3*C*. For the sake of completeness, in Fig. 3*C*, we report results for a smaller droplet size ($D_0 = 2.35$ mm) using the same flexible surface.

Collision Outcome. Using steel beams, we varied f_b by changing h_b and L_b, and we measured the collision outcome, namely the remaining droplet kinetic energy after recoil, E_{k1}. During the experiments, we set $D_0 = 2.23$ mm and $We = 78.8$, and we kept them constant throughout, resulting in $f_d = 1/\tau = 106$ Hz. Three beams were used with f_b equal to 0.27, 1.17, and 2.85 times f_d. We set m_b 3 to 6 times higher than m_d, so as to keep the effect on frequency shift due to the additional droplet mass minimum. We treated the beams with a hydrophobic coating nC2, and we fixed them on one side and simply supported the other, with no overhanging segment. The beam dimensions and characteristics are reported in Table 1.

We estimated E_{k1} by tracking its centroid. The elastic strain energy stored in the beam, E_{el}, was calculated by measuring its maximum deflection at the point of impact, δ_{max}, and substituting into $E_{el} \approx 0.5k_b\delta_{max}^2 - 1.282m_bg\delta_{max}$, where the second term accounts for the potential energy due to sagging; g is the gravitational acceleration, and the coefficient corrects for the mass being distributed over the beam (see *Beam Modeling*). Moreover, we calculated the total amount of energy available to the droplet, E_{tot}, as the kinetic energy just before impact plus the excess gravitational energy from the impact point to the point of maximum deflection, $E_{tot} \approx 0.5m_dU_0^2 + m_dg\delta_{max}$. Fig. 4 shows a plot of E_{k1} and E_{el} normalized by E_{tot} vs. f_b. Depending on the relation between f_b and f_d, and m_b and m_d, the substrate movement can act synergistically, passively, or destructively on E_{k1} (see Table 1 for f_b and m_b); E_{el} may return to the droplet or be dissipated by the beam oscillation. For beams with $f_b < f_d$, droplet recoil occurs during the downward motion of beam, decreasing E_{k1}. Alternatively, if $f_b \approx f_d$, the droplet recoils at the point of maximum velocity, recuperating E_{el} (see Movie S4). For beams with $f_b > f_d$, the dynamics resemble the rigid substrate case. Representative trajectories of the droplet centroid and beam impact point are shown in Fig. S4.

Interestingly, when $f_b \approx f_d$, E_{k1} is maximized and the repellency of the surface is enhanced, as more energy is available to the droplet for rebounding and recovering from possible partial impalement into the surface texture. Furthermore, for the same synchronized case, we observed a slight decrease in contact time, t_c. This reduction in t_c was found to be more pronounced for LDPE films under tension. By increasing the film strain, we detected jump of the droplets in a so-called "pancake" bouncing (11) (Fig. S5).

Butterfly Wing. An example from nature for the manifestation of enhanced hydrophobicity through high-$1/k$, low-ρ_A substrates was found in butterfly wings (*Lepidoptera*). We impacted water droplets onto the wings of three butterflies of different species (*Colias hyale*, *Callithea sapphire*, and *Inachis io*). See *Butterfly Wing* for their wetting properties.

The water droplet impact behavior on such wings, along with their surface micrographs, is shown in Fig. 5 *A* and *B* and Fig. S6. We supported the insect samples by a pin passing through their thorax, allowing their wings to deform freely under load. By adding a rigid glass support under the sample and filling the intermediate gap with water, we were able to reduce the flexibility of the wing and restrict its range of motion at will. For each butterfly species, we impacted droplets with $D_0 = 2.35$ mm at constant We, and we compared the effect of flexibility on the impalement resistance (see Movie S5). Fig. 5*C* shows Φ for the rigid and flexible cases. In the flexible case, Φ was 51 to 71% less compared with the rigid case, depending on the specimen.

Table 1. Beam dimensions for collision outcome experiment

Beam	L_b, mm	W_b, mm	h_b, μm	f_b, Hz	k_b, N/m	m_b, mg
1	50	10	20	29	1.0	33.7
2	24	10	20	124	9.8	16.2
3	19	10	30	297	66.9	19.2

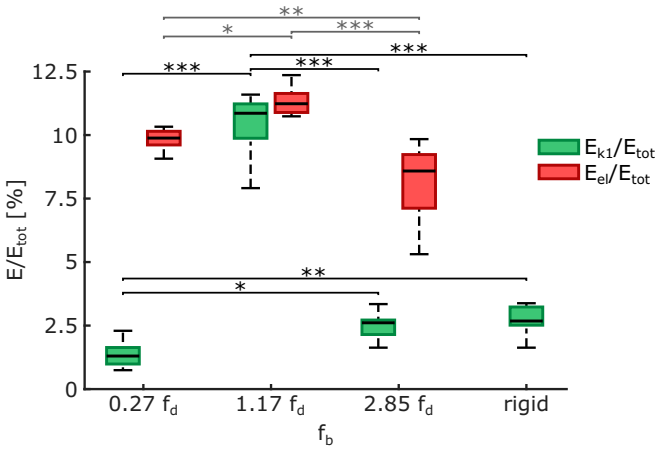

Fig. 4. Outcome of a droplet impact event for different beam resonance frequencies. Shown are residual kinetic energy of the droplet after rebound (E_{k1}, green) and strain energy of the beam at maximum deflection (E_{el}, red) normalized by the total available energy of the droplet before impact (E_{tot}) vs. f_b. The impact parameters are the same for all experiments ($D_0 = 2.23$ mm, $We = 78.8$). Box spans from the first to third quartile with Tukey style whiskers, and bold lines indicate population medians. Sample size (n) is eight repetitions per case. Significant differences are indicated by asterisks (black for E_{k1}, gray for E_{el}; *$P < 0.05$; **$P < 0.01$; ***$P < 0.001$).

Discussion

We have demonstrated that the flexibility of the substrate—controlled by ρ_A, k, and ζ—can enhance the superhydrophobic behavior of the surface. To enhance impalement resistance, the design rules were found to be $\rho_A << \rho D_0$, $k \approx \sigma$, and $\zeta \approx 0$. Satisfying these criteria facilitates the fast acceleration of the substrate to an incoming droplet during the early stage of the impact process. For minimizing droplet spreading and breakup, which occurs during the later stage of droplet–substrate impact, the above design rules also applied, with the added constraint that $f_b < f_d$. Separately, the criterion to maximize the kinetic energy of the droplet as it rebounds from the surface (important for liquid repellency) is then $f_b = 1/\tau$.

The mechanism behind this enhancement of hydrophobicity (minimizing Φ) through high-$1/k$, low-ρ_A substrates is connected to the momentum transfer during the droplet–substrate collision—from the droplet to the surface—quantified by the relative impact velocity. By measuring the U_s on impact, we showed that only substrates able to reach sufficient velocity at the initial moments after the collision can impede the impalement process. Because we detected motion even before contact, we speculate that the pressure of the air layer under the droplet is able to deform the substrate. Such intervening layers have been shown to affect the splashing dynamics (17, 29) and promote the droplet mobility in liquid films (30–32). Flexible films have been proposed to positively affect the dynamics of the air layer—by either reducing the maximum air pressure, reducing the relative impact velocity, or extracting kinetic energy from the droplet—and suppress splash (22). Due to the dual role that these intervening layers play in both splashing (17, 29) and impalement dynamics (14), one could expect flexible films to alter meniscus impregnation

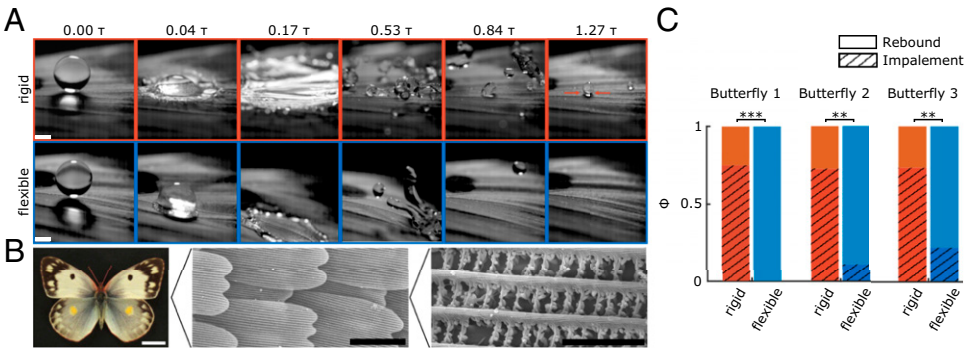

Fig. 5. Impact on butterfly wings. (*A*) Image sequences of a droplet ($D_0 = 2.35$ mm, $We = 389$) impacting on a supported and an unsupported butterfly wing of a specimen from the species *C. hyale*. Arrows indicate location of impalement. (Scale bar, 1 mm.) (*B*) Image of the butterfly and micrographs of the wings used for the droplet impact experiment in *A*. (Scale bar, left to right, 10 mm, 50 μm, and 5 μm.) (*C*) Φ for a droplet ($D_0 = 2.35$ mm) impacting on butterfly wings of the three tested species in supported (rigid) and unsupported (flexible) cases: Butterfly 1, *C. hyale*, $We = 389$; Butterfly 2, *C. sapphire*, $We = 568$; and Butterfly 3, *I. io*, $We = 401$. The sample size was $n \geq 9$. Significant differences are indicated by asterisks (**$P < 0.01$; ***$P < 0.001$).

behavior through a complex mechanism—based on compressibility effects (14), water hammer (13, 33), etc.—rather than a simple reduction of the dynamic pressure due to relative substrate motion (see *Dynamic Pressure*). However, balancing p_k with local capillarity can perhaps be used for an order of magnitude first estimate; this is an important aspect for future investigations.

Returning to splash suppression, because smaller droplets are harder to remove from the surface than larger ones (16), sustaining the droplet integrity can be advantageous for liquid repellency. For hydrophobic surfaces, splashing can also occur during the retraction phase, a pure wetting phenomenon provoked by the decrease in the dynamic contact angle, known as receding splashing (34). Reducing D_{max}/D_0 for a given We restricts the minimum lamella height and therefore the probability of droplet separation during the receding phase. For substrates with $f_b < f_d$, reduction in D_{max}/D_0 can be achieved. In such cases, the downward movement of the flexible substrate should persist across the entire spreading phase. If the δ_{max} is achieved before D_{max}, E_{el} returns to the droplet and participates in the spreading dynamics. This effect has been reported previously (21, 22), where, although the flexible substrates were able to absorb a considerable amount of E_{k0}, no difference on the D_{max}/D_0 was detected in comparison with the rigid case. Reduction in D_{max}/D_0 has, so far, only been reported on soft materials (35), and it is attributed to viscoelastic breaking, namely dissipation of energy in the contact line because of local deformation of the substrate, a mechanism different from the one proposed by the present study.

Furthermore, by tuning f_b, we can alter the droplet rebound dynamics. We have demonstrated that E_{k1} can be maximized by setting $f_b \approx f_d/C$, where C is an integer constant that, in this case, was set to unity. In this case, the droplet recoils from the surface while it is moving upward with its maximum velocity. The same cooperative effect is anticipated when $C > 1$ and $m_b < m_d$; however, E_{k1} should be reduced with successive substrate oscillations due to viscous losses and may therefore be undesirable. Additionally, for $f_b > f_d$, reduction in t_c can be achieved as shown by the LDPE films under strain (Fig. S5). The mechanism for this "spring-boarding" effect has recently been explained (36).

On the other hand, if the goal is minimization of E_{k1}, we showed that this can be achieved by setting $f_b < f_d$ and $m_b > m_d$. The underlying mechanism is that the droplet recoils upward while the surface is still moving downward; therefore, a considerable amount of energy is removed from the droplet, resulting in a reduced E_{k1} (see Movie S4). Additionally, when $m_b \approx m_d$, the droplet may not recoil from the surface after one droplet oscillation, because the surface is no longer sufficiently rigid to "break the symmetry." Rather, the droplet continues to oscillate on the moving surface and recoils as the substrate is moving upward—as shown by the steel beam case (see Movie S3). In this instance, E_{k1} is minimized through prolonged droplet–substrate contact (t_c). Here, $t_c > \tau$ and results in energy being dissipated by both the droplet and the beam. In the end, by either of the abovementioned mechanisms, what results is droplet "interception," an effect that has been observed for rain in the tree canopy (37).

Improved hydrophobicity, by making use of flexible surfaces, does apparently also come into play in nature; we observed this mechanism on butterflies. Our experiments show that flexibility reduces the probability of droplet impalement. Even though thermoregulated butterflies are rarely expected to fly during rainfall due to low sunlight conditions—because they can only reach the necessary body temperature for flight through solar irradiation (38, 39)—if a raindrop hit them, this might have disastrous effects on the filigree wing structure. Furthermore, flexibility prevents the raindrop from penetrating into the wing structure. In nature, a pinned raindrop on the butterfly wing could hinder flight or even cause wing scale delamination.

Materials and Methods

Droplet Impact Experimental Setup. See Fig. S2 *A* and *B* for a description of the droplet impact setup. For the experiments, we supported the surfaces by either fixing (clamping) both ends or fixing one and simply supporting the other. One of the supports was mounted on a linear stage, allowing us to vary L_s. For producing accurate droplet sizes, we used calibrated needles with repeatability error less than 5%. The needle was mounted on a vertical rail, which could be moved with a two-axis linear stage, to control the impact point. For steel beams, we always performed the impact at a distance $L_F = (2-\sqrt{2})L_s$ from the fixed support; this was the position for maximum theoretical deformation. For the LDPE films, impact points were random but near the middle area. A high-speed camera (Phantom V9.1; Vision Research) recorded the events (5,000 s^{-1} to 6,700 s^{-1}) in a backlit configuration.

Laser Doppler Vibrometry. We used a laser Doppler vibrometer (CLV-2534; Polytec) to measure the substrate velocity (Fig. S2*C*). A high-speed camera (FastCam SA1.1; Photron) recorded the impact event. Data acquisition of the vibrometer signal was carried out by an analog-to-digital converter (data acquisition; National Instruments) connected to a PC. Dedicated software (PFV Ver.351; Photron) acquired both the impact image sequence and the velocity measurement in sync.

Wettability Characterization. To assess the wettability of the coatings, we measured the apparent advancing (θ_a^*) and receding (θ_r^*) water contact angles by the stationary droplet method, whereby 5 μL to 10 μL of liquid was inflated (advancing) and deflated (receding) through a plastic, flat-tipped needle (GELoader Tips; Eppendorf) using a syringe pump. We made contact angle measurements with images captured with a detector (DCC1645C; Thorlabs) affixed with a standard zoom lens (MVL7000; Thorlabs) in a backlit-imaging configuration.

The measured values for the hydrophobic coatings are nC1 coating $\theta_a^* = 152° \pm 3°$ and $\theta_r^* = 145° \pm 5°$ and nC2 coating $\theta_a^* = 161° \pm 4°$ and $\theta_r^* = 158° \pm 4°$.

Butterfly Wing. The butterfly specimens were acquired from the entomological collection of Eidgenössische Technische Hochschule (ETH) Zürich, where they have been conserved in a dry state. For surface characterization, contact angles were measured on the butterfly wings, giving values of $\theta_a^* = 160° \pm 6°$ and $\theta_r^* = 155° \pm 6°$ for *C. hyale*, $\theta_a^* = 153° \pm 5°$ and $\theta_r^* = 149° \pm 6°$ for *C. sapphire*, and $\theta_a^* = 168° \pm 3°$ and $\theta_r^* = 163° \pm 3°$ for *I. io*.

Statistical Analysis. Statistical testing of the hypothesis that impalement resistance is affected by the flexibility of the substrate (LDPE film) was performed by the two-sided sign test. Statistical significance for the impalement resistance of butterfly wings in association with flexibility was tested using the Fisher's exact test. For comparing the population means between two groups, we used the two-sampled two-sided Student's *t* test. For comparing the population means among multiple groups, we used the one-way analysis of variance (ANOVA). Each group population that participated in either a Student's *t* test or an ANOVA was moreover tested for normality using the Anderson–Darling test. For comparison where we detected departures from normality (t_c vs. LDPE strain), we used nonparametric Kruskal–Wallis ANOVA. All statistical tests were performed at a significance level of $\alpha = 0.05$. All quantitative measurements reported are expressed as average values ±99% confidence intervals of the mean. The sample size is reported either in the legend or on the plot area of the presented graphs.

ACKNOWLEDGMENTS. We thank Tanmoy Maitra for his spadework, Gustav Graeber for doing surface morphology characterization, and Julian Marschewski for doing thickness measurements. We acknowledge the entomological collection of ETH Zurich (Rodney Eastwood) for donating the insect samples. Partial support of the Swiss National Science Foundation under Grant 162565 and the European Research Council under Advanced Grant 669908 (INTICE) is acknowledged. This study was also supported by ETH Zurich Postdoctoral Fellowship Program and the Marie Curie Actions for People COFUND Programme FEL-14 13-1 (to T.M.S.).

1. Quéré D (2005) Non-sticking drops. *Rep Prog Phys* 68(11):2495–2532.
2. Barthlott W, Neinhuis C (1997) Purity of the sacred lotus, or escape from contamination in biological surfaces. *Planta* 202(1):1–8.
3. Liu TL, Kim CJ (2014) Repellent surfaces. Turning a surface superrepellent even to completely wetting liquids. *Science* 346(6213):1096–1100.
4. Tuteja A, et al. (2007) Designing superoleophobic surfaces. *Science* 318(5856): 1618–1622.
5. Schutzius TM, et al. (2015) Physics of icing and rational design of surfaces with extraordinary icephobicity. *Langmuir* 31(17):4807–4821.
6. Clanet C, Beguin C, Richard D, Quéré D (2004) Maximal deformation of an impacting drop. *J Fluid Mech* 517:199–208.
7. Maitra T, et al. (2014) Supercooled water drops impacting superhydrophobic textures. *Langmuir* 30(36):10855–10861.
8. Latka A, Strandburg-Peshkin A, Driscoll MM, Stevens CS, Nagel SR (2012) Creation of prompt and thin-sheet splashing by varying surface roughness or increasing air pressure. *Phys Rev Lett* 109(5):054501.
9. Schutzius TM, et al. (2015) Spontaneous droplet trampolining on rigid superhydrophobic surfaces. *Nature* 527(7576):82–85.
10. Bird JC, Dhiman R, Kwon HM, Varanasi KK (2013) Reducing the contact time of a bouncing drop. *Nature* 503(7476):385–388.
11. Liu YH, et al. (2014) Pancake bouncing on superhydrophobic surfaces. *Nat Phys* 10(7): 515–519.
12. Gauthier A, Symon S, Clanet C, Quéré D (2015) Water impacting on superhydrophobic macrotextures. *Nat Commun* 6:8001.
13. Deng T, et al. (2009) Nonwetting of impinging droplets on textured surfaces. *Appl Phys Lett* 94(13):133109.
14. Maitra T, et al. (2014) On the nanoengineering of superhydrophobic and impalement resistant surface textures below the freezing temperature. *Nano Lett* 14(1):172–182.
15. Bartolo D, Josserand C, Bonn D (2005) Retraction dynamics of aqueous drops upon impact on non-wetting surfaces. *J Fluid Mech* 545:329–338.
16. Bartolo D, et al. (2006) Bouncing or sticky droplets: Impalement transitions on superhydrophobic micropatterned surfaces. *Europhys Lett* 74(2):299–305.
17. Liu Y, Tan P, Xu L (2015) Kelvin–Helmholtz instability in an ultrathin air film causes drop splashing on smooth surfaces. *Proc Natl Acad Sci USA* 112(11):3280–3284.
18. Gilet T, Bourouiba L (2015) Fluid fragmentation shapes rain-induced foliar disease transmission. *J R Soc Interface* 12(104):1092.
19. Zimmermann J, Reifler FA, Fortunato G, Gerhardt LC, Seeger S (2008) A simple, one-step approach to durable and robust superhydrophobic textiles. *Adv Funct Mater* 18(22):3662–3669.
20. Gilet T, Bush JWM (2009) The fluid trampoline: Droplets bouncing on a soap film. *J Fluid Mech* 625:167–203.
21. Mangili S, Antonini C, Marengo M, Amirfazli A (2012) Understanding the drop impact phenomenon on soft PDMS substrates. *Soft Matter* 8(39):10045–10054.
22. Pepper RE, Courbin L, Stone HA (2008) Splashing on elastic membranes: The importance of early-time dynamics. *Phys Fluids* 20(8):082103.
23. Soto D, De Larivière AB, Boutillon X, Clanet C, Quéré D (2014) The force of impacting rain. *Soft Matter* 10(27):4929–4934.
24. Gart S, Mates JE, Megaridis CM, Jung S (2015) Droplet impacting a cantilever: A leaf-raindrop system. *Phys Rev Appl* 3(4):044019.
25. Lamb H (1895) Surface waves. *Hydrodynamics* (Cambridge Univ Press, Cambridge, UK), pp 351–469.
26. Kolinski JM, et al. (2012) Skating on a film of air: Drops impacting on a surface. *Phys Rev Lett* 108(7):074503.
27. Li EQ, Thoroddsen ST (2015) Time-resolved imaging of a compressible air disc under a drop impacting on a solid surface. *J Fluid Mech* 780:636–648.
28. Laan N, de Bruin KG, Bartolo D, Josserand C, Bonn D (2014) Maximum diameter of impacting liquid droplets. *Phys Rev Appl* 2(4):044018.
29. Xu L, Zhang WW, Nagel SR (2005) Drop splashing on a dry smooth surface. *Phys Rev Lett* 94(18):184505.
30. Gilet T, Bush JWM (2012) Droplets bouncing on a wet, inclined surface. *Phys Fluids* 24(12):122103.
31. Hao C, et al. (2015) Superhydrophobic-like tunable droplet bouncing on slippery liquid interfaces. *Nat Commun* 6:7986.
32. Hao C, et al. (2016) Bioinspired interfacial materials with enhanced drop mobility: From fundamentals to multifunctional applications. *Small* 12(14):1825–1839.
33. Kwon HM, Paxson AT, Varanasi KK, Patankar NA (2011) Rapid deceleration-driven wetting transition during pendant drop deposition on superhydrophobic surfaces. *Phys Rev Lett* 106(3):036102.
34. Rioboo R, Tropea C, Marengo M (2001) Outcomes from a drop impact on solid surfaces. *At Sprays* 11(2):155–165.
35. Rioboo R, et al. (2010) Drop impact on soft surfaces: Beyond the static contact angles. *Langmuir* 26(7):4873–4879.
36. Weisensee PB, Tian J, Miljkovic N, King WP (2016) Water droplet impact on elastic superhydrophobic surfaces. *Sci Rep* 6:30328.
37. Livesley SJ, Baudinette B, Glover D (2014) Rainfall interception and stem flow by eucalypt street trees—The impacts of canopy density and bark type. *Urban For Urban Green* 13(1):192–197.
38. Kingsolver JG (1983) Thermoregulation and flight in *Colias* butterflies—Elevational patterns and mechanistic limitations. *Ecology* 64(3):534–545.
39. Wickman PO (2009) Thermoregulation and habitat use in butterflies. *Ecology of Butterflies in Europe*, eds Settele J, Shreeve T, Konvička M, van Dyck H (Cambridge Univ Press, Cambridge, UK), pp 55–61.
40. Mao T, Kuhn DCS, Tran H (1997) Spread and rebound of liquid droplets upon impact on flat surfaces. *AIChE J* 43(9):2169–2179.
41. Tiwari MK, Bayer IS, Jursich GM, Schutzius TM, Megaridis CM (2010) Highly liquid-repellent, large-area, nanostructured poly(vinylidene fluoride)/poly(ethyl 2-cyanoacrylate) composite coatings: Particle filler effects. *ACS Appl Mater Interfaces* 2(4): 1114–1119.
42. Antonini C, et al. (2014) Unraveling wetting transition through surface textures with X-rays: Liquid meniscus penetration phenomena. *Sci Rep* 4:4055.
43. Verho T, et al. (2012) Reversible switching between superhydrophobic states on a hierarchically structured surface. *Proc Natl Acad Sci USA* 109(26):10210–10213.
44. Rioboo R, Voué M, Vaillant A, De Coninck J (2008) Drop impact on porous superhydrophobic polymer surfaces. *Langmuir* 24(24):14074–14077.
45. Timoshenko S, Gere JM (2009) Beam-columns. *Theory of Elastic Stability* (Dover, Mineola, NY), pp 1–45.
46. Barentse Wm, Heikens D (1973) Mechanical properties of polystyrene low density polyethylene blends. *Polymer* 14(11):579–583.
47. Bathe KJ, Bolourchi S (1979) Large displacement analysis of 3-dimensional beam structures. *Int J Numer Methods Eng* 14(7):961–986.
48. Pica A, Wood RD, Hinton E (1980) Finite-element analysis of geometrically nonlinear plate behaviour using a Mindlin formulation. *Comput Struc* 11(3):203–215.
49. Attane P, Girard F, Morin V (2007) An energy balance approach of the dynamics of drop impact on a solid surface. *Phys Fluids* 19(1):012101.
50. Richard D, Quéré D (2000) Bouncing water drops. *Europhys Lett* 50(6):769–775.